Applied Ocean Research 170 (2026) 105033

Contents lists available at ScienceDirect

Applied Ocean Research

journal homepage: www.elsevier.com/locate/apor

Research paper

External Acoustic Black Holes to reduce structural vibration and radiated sound by a plate in contact with water

Giovanni Rognoni [a,*], Jacopo Fragasso [b], Marco Biot [a], Lorenzo Moro [b]

[a] Department of Engineering and Architecture, University of Trieste, Via Alfonso Valerio 7/4, Trieste, 34127, Italy
[b] Department of Ocean and Naval Architectural Engineering, Faculty of Engineering and Applied Science, Memorial University of Newfoundland, St John's, Newfoundland and Labrador, A1B3X5, Canada

ARTICLE INFO

Keywords:
Metamaterial
Underwater noise
Radiation efficiency
Deep tank
Hull radiation

ABSTRACT

Ship noise arises from various sources, including propeller cavitation, hydrodynamic flow, and onboard machinery. Vibrations from rotating and reciprocating machines can propagate through the ship's structure and radiate into the marine environment, significantly contributing to underwater noise pollution. This study investigates the potential of Acoustic Black Holes (ABH) to mitigate structural vibrations and, consequently, reduce underwater radiated noise. ABHs are passive vibration-damping devices that utilize a unique mechanism to concentrate and dissipate vibrational energy. While their potential on structures in air is recognized, the effect on structures in contact with water has yet to be investigated. A series of experiments was conducted on a rectangular steel plate subjected to controlled excitation using an electrodynamic shaker. The results show a noticeable reduction in structural vibration levels across a broad frequency range (50–5000 Hz) with the implementation of ABHs. However, this reduction does not directly translate into a corresponding decrease in underwater radiated noise. The inconsistency between vibration reduction and acoustic radiation was analysed and discussed. These findings provide insight into the effectiveness and limitations of ABHs in underwater noise mitigation strategies.

1. Introduction

Sound is essential for the conservation of marine species, as they use it for navigation, habitat selection, communication, mating, sensing, echolocation, and social interaction. These activities are endangered by anthropogenic noise deriving from human activities. Commercial and recreational shipping, oil and gas exploration and production, naval operations, fishing, research, and construction imperil life at sea (Hildebrand, 2009). The efforts being made to reduce ships' impact are increasing. Organizations are implementing regulations promoting the reduction of Underwater Radiated Noise (URN) by ships. The International Maritime Organization (IMO) recently reviewed the guidelines on URN issued in 2014 (IMO, 2014), showing the field is constantly developing (IMO, 2023). Through its Specialist Committee on Hydrodynamic Noise, the International Towing Tank Conference (ITTC) published a report containing some recommendations and a detailed review of regulations, assessment criteria, and model scale measurement (Bosschers et al., 2021). The EU recently published a commission notice setting limits for impulsive and continuous URN (EU Commission, 2024); these limits are yet to be defined. Most classification societies have their rules to assess the acoustic underwater footprint of ships (Det Norske Veritas Germanischer Lloyd, 2010; Lloyd's Register, 2018; Bureau Veritas, 2018; Korean Register, 2021; Registro Italiano Navale, 2022; CR Classification Society, 2023; American Bureau of Shipping, 2024). All these regulations are based on ISO (2016) and ISO (2019), which standardize the underwater measurement procedures for deep water. In Canada, the Federal Government recently published the Ocean Noise Strategy (Government of Canada, 2024). The Strategy outlines a group of goals and avenues of action to inform a Federal Action Plan to understand and reduce underwater noise levels and their impact on marine life.

Depending on the target source, different actions can be taken to reduce the ship's impact. The main sources of noise and vibrations on board are machinery (Park et al., 2024) and propeller (Tani et al., 2016; Gaggero et al., 2025). Smith and Rigby (2022) illustrated an exhaustive list of countermeasures, examining underwater noise sources, discerning principally between hydrodynamic noise generated by the propeller and noise generated by the machinery. Other possible countermeasures are reducing speed, re-routing, and regular maintenance (IMO, 2023) or using alternative systems as active-noise control actuators (Tian et al., 2025).

* Corresponding author.
E-mail address: giovanni.rognoni@dia.units.it (G. Rognoni).

https://doi.org/10.1016/j.apor.2026.105033
Received 23 September 2025; Received in revised form 12 January 2026; Accepted 16 March 2026
Available online 17 March 2026

Among new solutions showing potential in decreasing structural vibration, and therefore radiated noise from ships, there is the Acoustic Black Hole (ABH). First introduced by Minonov (1988), who described its working principle, the interest in this solution has grown significantly in the last twenty years (Pelat et al., 2020). Nowadays, more than five hundred papers can be found on the subject, and the number of patents filed worldwide exceeds fifty (Bschorr and Raida, 2022). ABHs work based on the principle of gradually reducing the thickness of a structure, typically a plate or beam, towards a zero-thickness edge, following a specific power-law profile. As the thickness decreases, the velocity of flexural waves tends to zero, causing the energy not to reach the end and becoming trapped. The described mechanism refers to the ideal case; however, in practical applications, it is not possible to manufacture a zero-thickness termination. A thin layer of damping material is usually applied at the ABH tip to achieve energy dissipation. This combination of wave slowing and localized damping leads to a substantial attenuation of vibrational energy.

ABHs can be internal or external. Internal ABHs are indentations carved inside a structure. Flexural waves travelling through the structure encounter the ABH along their path and are trapped. This solution was largely studied (Conlon et al., 2015; Feurtado and Conlon, 2016, 2017; Ji et al., 2019; Du et al., 2019; Deng et al., 2021) and proved to be the most effective (Krylov and Winward, 2007; Krylov, 2014). However, it has the drawback of compromising structural integrity, making it difficult to be implemented on ships, as it would require a complete overhaul of the structural design methods. External ABHs are typically beams attached externally to a host structure. Part of the energy introduced by the vibrational source is absorbed by the ABH and then dissipated. As these devices are externally attached, their location on the host structure is very important, and their performance is influenced by it. Moreover, they have their own dynamic, which interacts with that of the host structure, possibly leading to unexpected modes introduced in the system.

The first of these external ABH was introduced by Zhou and Cheng (2018). They proposed an ABH-featured Resonant Beam Damper (ABH-RBD) that combined the effect of a tuned vibration absorber with the ABH dissipation effect. Other shapes for external ABH vibration absorbers have been investigated: circular (Ji et al., 2021, 2022; Zhao et al., 2024) or double-sided (Li et al., 2022; Wen et al., 2024). A spiral ABH has been developed by Lee and Jeon (2017, 2021), who demonstrated that the effect achieved with this type of solution is similar to that achieved with a standard ABH profile. Subsequently, Park et al. (2022) performed a study on the vibration reduction of a plate in the 0–500 Hz frequency range using the spiral ABH, optimizing parameters, number, and position on the surface. Further studies on spiral ABH were recently presented by Jeon et al. (2024).

Before the ABH principle was stated, the United States Navy performed similar research on prototypes they called waveguide absorbers. Ungar and Kurzwell (1984) demonstrated that attaching external beams with damping coatings to a metal plate could double the plate loss factor. They also further noted that tapered beams enhanced the dissipation effect, arriving at conclusions similar to Mironov's. Lee (1988) and Watson (1989) experimentally tested linear beam waveguide absorbers and refined Ungar and Kurzwell's work. Whether the US Navy's studies led to practical applications of waveguides in naval vessels remains unclear.

Much of the experimental activity on external ABHs was performed by placing them on beams and plates. To the best of the authors' knowledge, most of these tests were carried out in air (or vacuum), while a few considered the decrease of noise radiation in water. A first approach was proposed by Deng et al. (2023), who calculated the underwater sound radiation from a thick plate with an ABH embedded in it using Mindlin's theory. In the paper the authors state: "The underwater sound radiation behaviour of ABH structures has never been reported, and the physics is unclear". The paper by Deng et al. considers ABH obtained within the structure, and not attached externally. Two more recent papers from Zhang et al. (2024) and Gao et al. (2025) are related to using ABH in water. Zhang et al. studied a tree-shaped ABH module to increase underwater surface noise absorption and decrease sound tracing. Gao et al. placed a series of external ABHs on an internal panel of an underwater cylinder reinforced structure to decrease its vibration. However, only structural accelerations were measured, no measurement of the radiated noise was performed.

In this paper, an application of external ABHs to investigate their URN mitigation effect on a steel plate was performed. The study was conceived as the first step towards future implementation of this technology on ship hulls. An experimental test was performed in a tank filled with water, keeping a rectangular steel plate in two conditions: air and with a side in contact with the water. The plate was elastically suspended and excited by an impulsive force through an electrodynamic shaker. The results obtained were evaluated by measuring the Mean Square Velocity (MSV) reduction obtained on the plate surface after installing one to four ABHs. The radiated pressure in the tank was also measured.

The paper is organized as follows: Section 2 shows the methodology used for the experiment: the basic theory governing sound radiation by plates (2.1), the experimental setup (2.2), the design of the ABH prototypes (2.3), their modal characteristics (2.4), and the criterion used to select their position (2.5). The section is concluded with the test objectives (2.6). Section 3 shows the experiment outcomes, which are discussed in Section 4. The section presents: the ABH performance in vibration reduction (4.1), the effect of the interaction with the water (4.2), the decrease of radiated noise (4.3), and the limitations of this study (4.4). Section 5 summarizes this work and highlights the main findings.

2. Methods

2.1. Radiation by plates

The radiation efficiency (or normalized radiation resistance) σ of a vibrating plate is obtained by the ratio between the radiation resistance R and the product between the fluid density ρ and speed of sound c, and by the contact area between fluid and structure S (Hambric and Fahnline, 2016):

$$\sigma = \frac{R}{\rho c S} \tag{1}$$

The radiation resistance is obtained dividing the radiated power P_{rad} by the spatially-averaged mean-square velocity MSV:

$$R = \frac{P_{rad}}{MSV} \tag{2}$$

By substituting Eq. (2) into Eq. (1), we obtain the typical formulation for σ and P_{rad}:

$$\sigma = \frac{P_{rad}}{\rho c S MSV} \qquad P_{rad} = \rho c S \sigma \cdot MSV \tag{3}$$

Many authors estimated the sound power level in a reverberant field tank, most recently (Fragasso et al., 2024; Lee et al., 2023). The equation to experimentally calculate P_{rad}, measuring the radiated pressure at a point in the tank, is:

$$P_{rad} = \frac{10^{\frac{SPL_{rev}}{10}} V}{1.58 \cdot 10^{20}\, T_{60}(1-\bar{\alpha})} \tag{4}$$

where V and A are the volume and the internal area of the tank, respectively, $\bar{\alpha}$ is the surface-averaged tank absorption coefficient, and the quantity T_{60} is the reverberation time in the tank, generally varying in frequency, and indicated by Jones and Hoefs (1996) as:

$$T_{60} = \frac{0.0373 V}{\bar{\alpha} A} \tag{5}$$

The sound power level SPL is the sound pressure level of spatially averaged RMS sound pressure due to reverberant field (ref 10^{-6} Pa).

Table 1
Frequency-dependent overall absorption coefficient of the water tank (Islam, 2022).

f	α	f	α	f	α
400	0.025	1000	0.0703	2500	0.0827
500	0.03	1250	0.069	3150	0.0802
630	0.0613	1600	0.1112	4000	0.1036
800	0.0654	2000	0.1256	5000	0.1135

(a) (b)

Fig. 1. (a) One of the two plates used in the lab tests, positioned on side of the deep tank during set up preparation. The circles indicate the load cell, accelerometers fixed on set 1 (right side), and the eyebolt suspension system; (b) deep tank facility. The red circle indicates the suspension beam for the hydrophones.

The Schroeder frequency provides the lower limit over which the pressure field can be considered reverberant:

$$f_S = \frac{1}{2}\sqrt{N}\sqrt{\frac{c^3\, T_{60}}{3\, ln(10)\, V}} \tag{6}$$

where c is the fluid speed of sound, and N is the number of overlapping modes.

2.2. Experiment setup

The tank used for the tests is a 3.65 m x 3.65 m x 3.65 m concrete square tank, in which the water level could be adjusted. The deep tank facility belongs to the Fluids Laboratory at Memorial University of Newfoundland, Canada. According to Islam (2022) and Fragasso et al. (2024), who performed experiments in the same facility, the tank has an average value of reverberation time of 0.32 s; the absorption coefficient is provided in Table 1.

Two identical plates were used in the experiment. One of them is shown in Fig. 1(a). The deep tank facility where the experiments were performed is shown in Fig. 1(b). The plates measured 1400 × 1000 mm with a thickness of 6.35 mm. The material was steel, with an estimated density of approximately 7860 kg/m^3, having a total mass of 69 kg.

The plates were hung through an elastic rope passing through four eyebolts placed at each corner and suspended using a crane as shown in Fig. 2(a). When in contact with the water, the inclination of the plate was carefully controlled to maintain it parallel to the liquid surface. Due to manufacturing and constraints, the plates were slightly bent at the four corners, introducing some experimental uncertainties. To ensure that the entire bottom of the plate was fully in contact with the water, the plate was lowered slightly below the water level, and a styrofoam boundary was created to prevent water from flooding the dry surface, as shown in Fig. 1(a). The plate was excited by a PCB Piezotronics electrodynamic shaker (Model 2060E) connected through a steel stinger to a PCB Piezotronics load cell (Model 208C02) to measure the excitation force. The amplifier used was a PCB Piezotronics 2050E09 model driven by a National Instruments 9260 voltage output module controlled by a LabView script.

A set of eight PCB Piezotronics Model 352C33 accelerometers was used to measure accelerations at sixteen locations, divided into two sets, equally spaced on the plate surface. Each location was in the geometrical centre of a 250 x 350 mm square area. The data acquisition system used is National Instruments 9234. Two Ocean Sonics Model icListen RB9-ETH hydrophones were deployed in the tank to measure the underwater sound pressure. The first, P1 (red circle in Fig. 2(b)), at a depth of 1.52 m and from 0.81 m from the right end corner in both directions; the second, P2 (yellow circle in Fig. 2(b)), at a depth of 2.44 m, at 0.81 m from the border parallel to the rod suspending the hydrophones and 2.08 m from the side right border.

The excitation force was applied as indicated in Fig. 3, in position $x = [715, 200, 0]$ from the origin of the frame of reference. The figure also shows the locations of the sixteen measurement points, divided by measurement set. The white noise signal was subdivided into two profiles: profile A from 10 to 400 Hz and profile B from 400 to 5000 Hz. Fig. 4 shows two typical coherence signals obtained for two accelerometers for profiles A and B. The resolution used to compute the spectra was 0.1 Hz for profile A, and 1 Hz for profile B, adopting a Hanning window with an overlap of 75% for averaging. The time signals recorded were 180 s long.

2.3. ABH design

Two models of acoustic black holes were used in this research. The design was based on a parameter called cut-on frequency (f_{cut-on}). This frequency represents the limit above which the flexural waves entering the ABH become propagative, while below this specific value, these waves are evanescent and the ABH mechanism is not enabled (Aklouche et al., 2016). When propagative waves reach the tip, they generate local internal resonances, called trapped modes, which are the maximum energy scattering frequencies. The values of the truncation, and therefore the net length of the ABH, affect the frequencies of these modes.

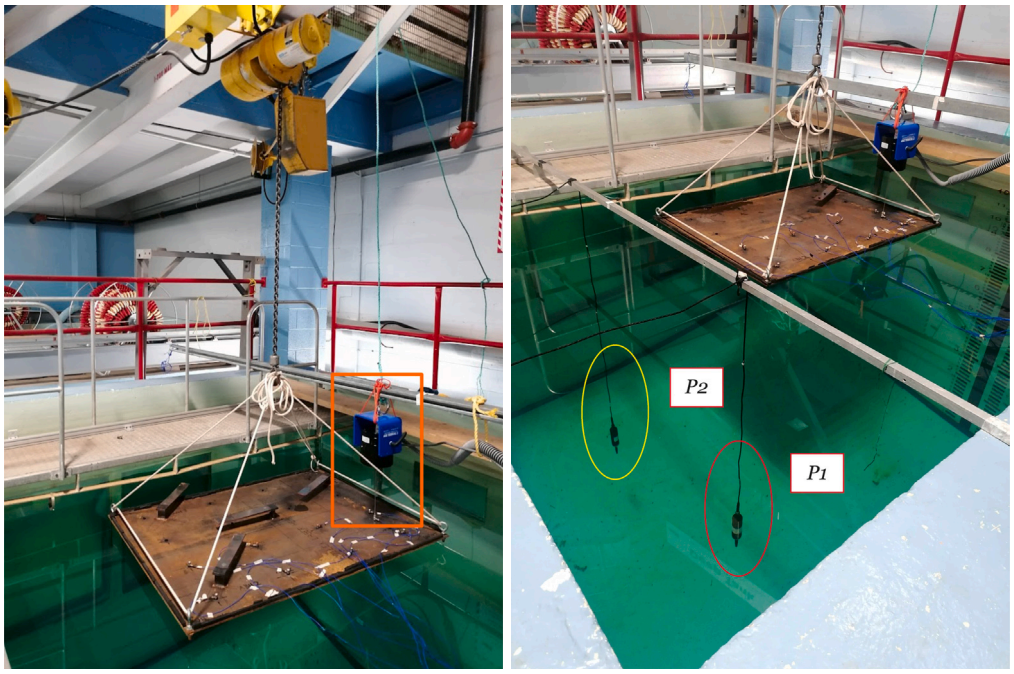

Fig. 2. Experimental setup: (a) plate suspended by the overhead crane and connected to the electrodynamic shaker; (b) disposition of the hydrophones: P1, red circle, and P2, yellow circle.

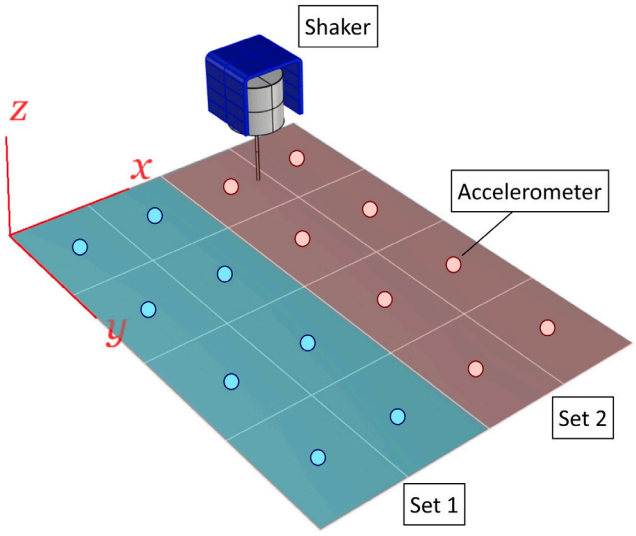

Fig. 3. Drawing of the plate with indication of reference system, shaker, and accelerometer positions divided in two measurement sets: set 1 (cyan) and set 2 (red)

Elongating the termination makes the object more flexible, shifting more of these modes to lower frequencies.

A first approach to calculate the cut-on frequency was developed by Aklouche et al. (2016) using the linear Kirchhoff model. Hence, their study is valid when these hypotheses are valid: (i) shear contribution in the wave propagation is negligible, which is valid when $\lambda \gg 6h$; (ii) out-of-plane displacement is supposed to be small compared with the thickness of the plate, $w/h \ll 1$. The cut-on frequency is calculated as:

$$f_{cut-on1} = \frac{h_0}{2\pi L^2}\sqrt{\frac{E[n^2(n^2-30\nu+22)-24\nu+40]}{12\rho(1-\nu^2)}} \tag{7}$$

This equation was obtained for a power law coefficient m equal to 2. L is the length of the ABH and h_0 is the starting thickness of the original beam/plate. E, ν, and ρ are the elastic modulus, the Poisson's coefficient, and the density of the plate, respectively. n is the circumferential order of Bessel's function used to solve the governing equations of the problem.

A second equation was developed by Lee and Jeon (2021). The authors derived the standard ABH's cut-on frequency from the Euler–Bernoulli equation's exact solution (Lee and Jeon, 2019).

$$f_{cut-on2} = \frac{1}{2\pi}\sqrt{\frac{E}{12\rho}}h_0\left(\frac{1.94}{L}\right)^2 \tag{8}$$

Using the same material, length, and thickness, Eq. (7) with $n = 0$ gives a cut-on frequency approximately 1.6 times higher than Eq. (8), resulting in a more conservative approach.

The ABHs used in this paper were made of steel and manufactured through a milling process by the Memorial University of Newfoundland Technical Service (four for each model). We selected steel for ease of integration and compliance with fire regulations on board ships covered by the SOLAS convention. Four specimens were created for each model. The geometrical data is shown in Fig. 5. Both models have a width of 50 mm. Model 2 has the same dimensions as Model 1, with the difference that a 100 mm extension was added to the tip to try to shift more modes of vibration to the low-frequency range, enhancing the low-frequency damping of the ABH. The estimated cut-on frequency selected is 108.4 Hz according to Eq. (7) and 68 Hz according to Eq. (8). Fig. 6 shows two of the eight ABH prototypes manufactured. To enhance the ABH's effectiveness, a 2 mm VEM layer was applied to the ABH along its entire length (excluding the connecting extension). A 2 mm steel plate was placed as a constraining layer. The total weight is 1.00 kg for Model 1 and 1.17 kg for Model 2.

2.4. Modal analysis

An experimental modal analysis was performed to investigate the flexural modes of the ABHs. The ABHs were suspended using two thin nylon wires. The hammer used was a PCB Piezotronics Model 086C03,

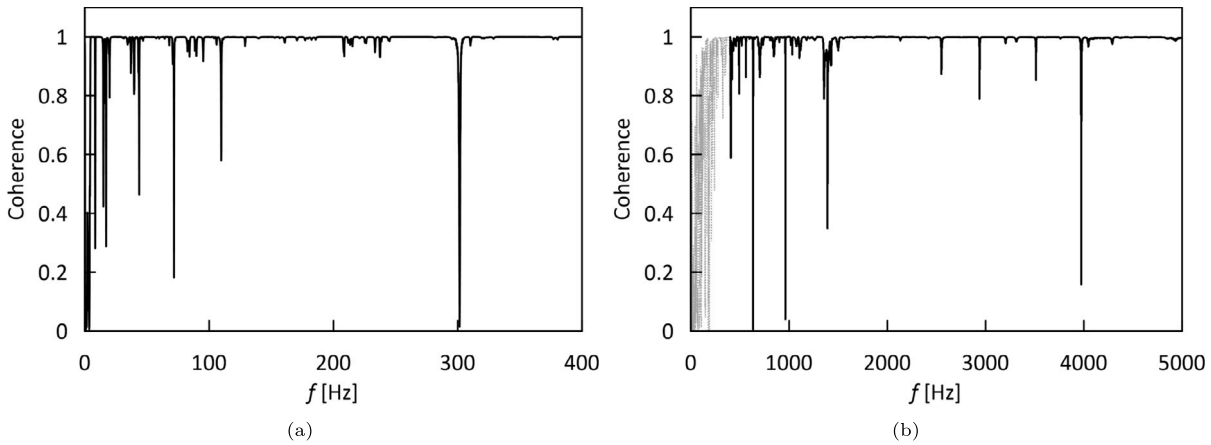

Fig. 4. Typical coherence between input and output signal obtained on the measurements point: (a) Profile A 0–400 Hz; (b) Profile B 400–5000 Hz.

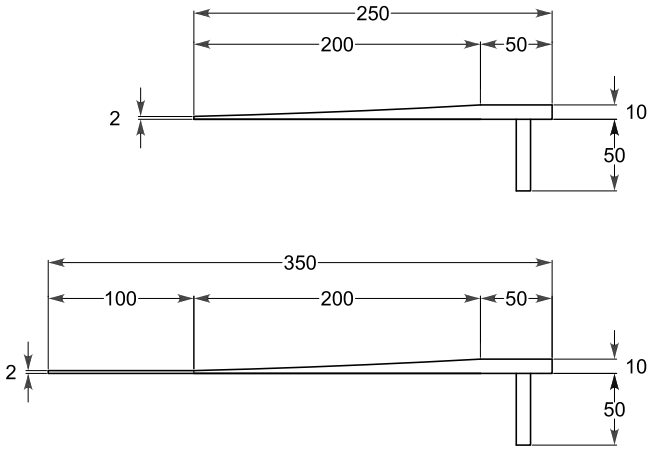

Fig. 5. Longitudinal view of ABH Model 1 and Model 2 made by a tapered beam without and with constant-thickness extension and the vertical support (dimensions quoted in mm).

the accelerometers used were PCB Piezotronics Model 352C33, and the acquisition systems was the National Instruments 9234 module. The analysis was performed using the rowing accelerometer technique, obtaining the acceleration-force transfer function in 7 points for Model 1 and 10 points for Model 2.

A FE model was developed using Hexagon Nastran to replicate the experimental modal analysis and obtain the modes when the base of the ABH is clamped. This condition was assumed as more similar to that of the ABH when welded on the host plate. The elements' length and height varied between 1 and 2 mm, with a width of 1 mm. The maximum aspect ratio was kept below 3. The models' VEM layer and the constraining plate were discretized using 3 elements along the thickness, which led to a higher maximum aspect ratio (around 7) in the area far from the ending tip where the elements' length increases. The FE models for ABH are presented in Fig. 7.

Table 2 shows the frequencies of the bending modes of vibration of the two ABH models calculated by hammer test. The experimental results are indicated by the columns "Exp Free", meaning experimental and free condition. The columns "Num" indicate the modal frequencies estimated by finite element analysis in "Free" condition to validate the mode and in "Clamped" condition which refer to the case where the base of the ABH is blocked. The columns "Error" indicate the error between the free experimental and numerical modal frequencies. The FE model parameters were adjusted to keep the error below 5%. The table shows that the 100 mm extension applied to Model 2 increases the number of modes from five to eight in the interval 0–5000 Hz.

2.5. ABH position

One of the parameters affecting the ABH performance when applied to a host structure is its location, which defines which modes are affected by the ABH. For dynamic vibration absorbers, the best location corresponds with the points of maximum displacement. For vibration waveguides, it was argued that the best location corresponds with the maximum vibrational energy for the cross-sectional area (Park et al., 2022). If this is the case, a method based on Structural Intensity (SI) can be used. Structural Intensity $\vec{I}(t)$ is defined as the product between the stress tensor $\hat{\sigma}(t)$ and velocity $\vec{v}(t)$ as per in Eq. (9):

$$\vec{I}(t) = -\hat{\sigma}(t)\vec{v}(t) \tag{9}$$

The same equation can be expressed by formulating each kth component of the structural intensity vector:

$$I_k(t) = \sum_{j=1,2,3} -\sigma_{kj}(t)\, v_j(t) \qquad k = 1,2,3 \tag{10}$$

Structural Intensity (Pavić, 1976) was revealed to be a useful tool to identify the points where to place a damper mechanism (Spalding and Mann, 1995; Kruger et al., 1997). The present paper used the SI method to define the position of the ABHs. Its value across the host structure was estimated following the SI formulation of finite elements given by Gavrić and Pavić (1993). The analysis was performed by MSC Nastran on a plate with the same dimensions as those tested, using square 2D elements of 10 mm. The FE model was updated to match the experimental response according to Rognoni et al. (2024).

The structural intensity method is a deterministic method most indicated for low frequencies, as it is based on FE. The Schroeder frequency for the tank was estimated to be around 2000 Hz; however, previous work showed good agreement between numerical results and experimental data starting from 500 Hz (Fragasso et al., 2024). This incompatibility led us to choose these four third-octave bands, representing the best compromise between obtaining a consistent sound pressure measurement in water and using the SI method to place the ABHs on the host structure. The positions of the four ABHs were decided by calculating the SI field of four third-octave bands: 800, 1000, 1250, and 1600 Hz (Fig. 8).

The SI pattern is not well-defined due to the high modal density. The energy is distributed diffusely on the surface, making it challenging to identify a clear energy hotspot where to install the ABHs. For the 800, 1000, and 1250 Hz third-octave bands, the locations of the maximum value of SI were selected, and the ABHs were positioned. As the 1600 Hz SI field (Fig. 8(d)) showed no hotspots, the fourth ABH was placed at a point of supposed low vibrational energy for all four bands studied to investigate whether this intervention would impact them. Theoretically, the ABH should have little or no effect when placed in

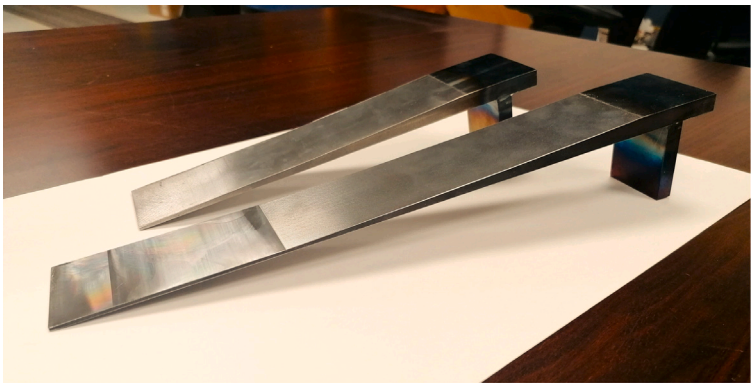

Fig. 6. ABH Model 1 and Model 2 prototypes manufactured for the experiment.

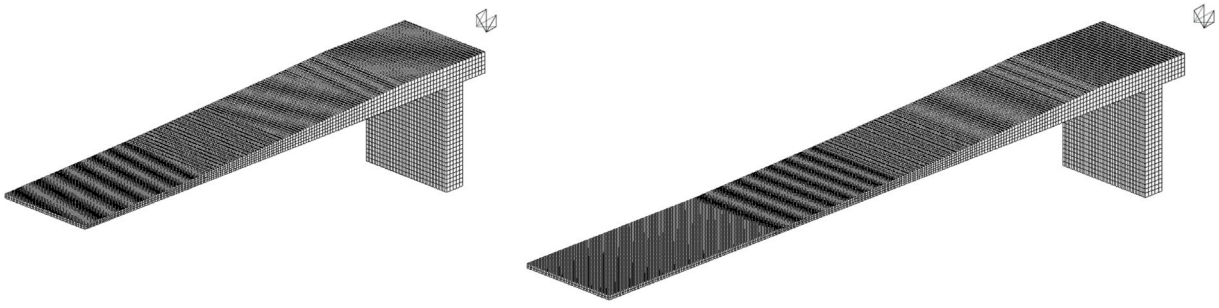

(a) (b)

Fig. 7. FE models of (a) ABH Model 1 and (b) Model 2.

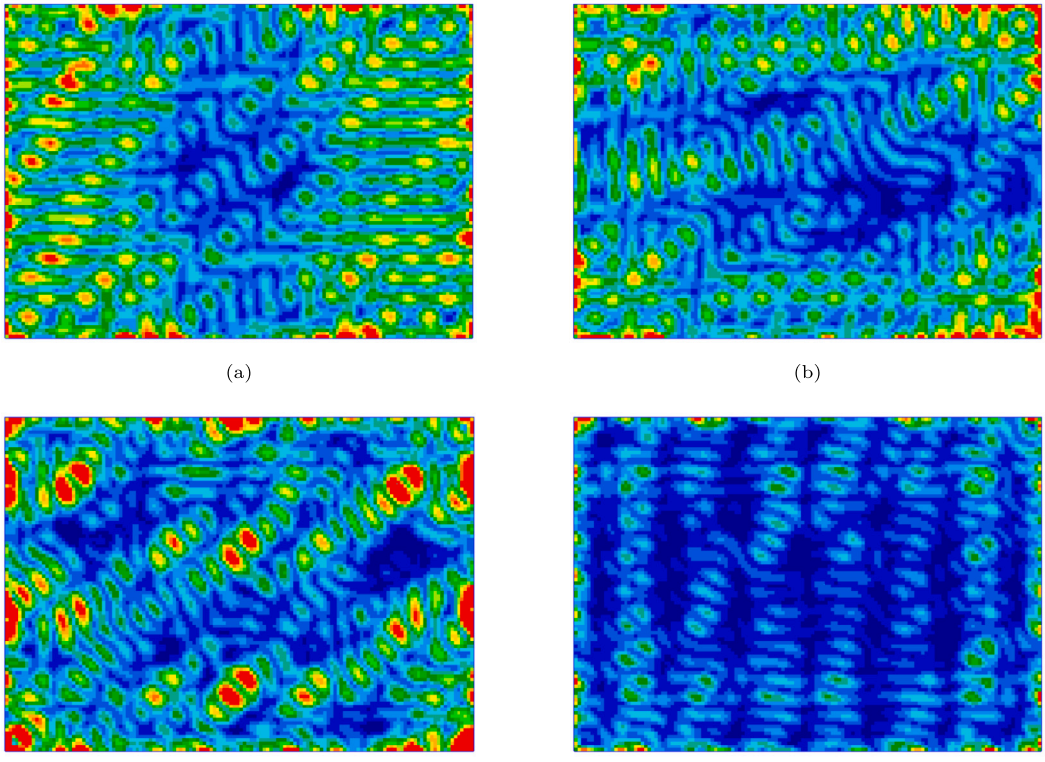

(a) (b)

(c) (d)

Fig. 8. Reactive SI fields for the third-octave bands investigated: (a) 800 Hz, (b) 1000 Hz, (c) 1250 Hz, and (d) 1600 Hz. Warmer colours indicated areas of higher average energy.

Table 2
Modal frequencies of the ABHs.

Mode	Model 1				Model 2			
	Exp Free	Num Free	Error	Num Clamped	Exp Free	Num Free	Error	Num Clamped
	Hz	Hz	%	Hz	Hz	Hz	%	Hz
1	443.0	439.9	0.7	490.3	170.1	167.7	1.4	221.2
2	1079.8	1081.4	−0.1	899.7	435.5	431.9	0.8	466.2
3	1853.2	1867.3	−0.8	1437.4	835.9	837.9	−0.2	749.2
4	2889.5	2900.6	−0.4	2282.4	1327.3	1313.6	1.0	1090.9
5	4238.9	4328.2	−2.1	4000.1	1850.7	1854.2	−0.2	1544.4
6	/	/	/	/	2567.2	2571.2	−0.2	2302.9
7	/	/	/	/	3329.4	3336.9	−0.2	3142.7
8	/	/	/	/	4156.6	4254.4	−4.0	4006.9

Table 3
Positions of the four ABH installed. The coordinates indicate the distance between the origin indicated in Fig. 3 and the centre of the cross-sectional area of the ABH supporting bracket.

f-band [Hz]	Position	x [mm]	y [mm]
800	S1	230	120
1000	S2	780	1180
1250	S3	170	1170
1600	S4	440	650

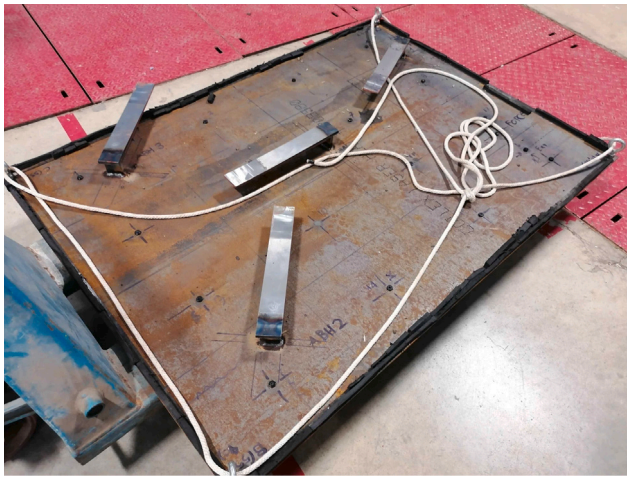

Fig. 9. Position of the ABHs welded on the plate.

such a position. Table 3 specifies the coordinates of the ABHs according to the frame of reference shown by Fig. 3. The origin is located in the lower left corner of Fig. 9, which shows plate 1 with four ABH Model 2 welded on. The connection was made by continuous welding.

2.6. Objectives and tests performed

The experiment described in this paper was designed to prove the effectiveness of the application of multiple ABHs on a plate. The test was performed in two configurations: air (dry condition) and keeping one face of the plate in contact with water (wet condition). The wet configuration test was also designed to assess the ABH impact on underwater radiated noise. The following list contains the principal objectives that were pursued while performing the experiment:

1. Evaluate the vibration mitigation performance of ABH Models 1 and 2 in dry and wet conditions across the frequency spectrum investigated: Low frequency 50–400 Hz; high frequency 400–5000 Hz
2. Investigate any effect of the water on the performance of the ABHs
3. Measure and analyse the underwater pressure levels radiated by the plate with and without ABHs, with particular focus on the 800, 1000, and 1250 Hz third-octave bands used for select ABH positions

Table 4 shows the list of tests performed. For practical reasons, Model 1 was tested on plate 2, while Model 2 was tested on plate 1. As Model 2 was expected to be the most effective, it was used to study the additive effect obtained by progressively increasing the number of ABHs installed. Model 1 was used only to estimate the overall effect when four devices are used.

The reproducibility of the test was investigated by repeating the trials in some configurations. For each third-octave band, the MSV (spatial average of squared velocities measured at 16 locations) was subsequently averaged across the repeated experimental trials. To evaluate reproducibility, we used the coefficient of variation (COV), assuming a threshold of 0.3, which is consistent with values found in vibration measurement literature (Tao et al., 2025). The values obtained from the repeated trials are consistent with the combined effects of modal spatial variability and broadband frequency integration. Table 5 shows the average COV for the repeated tests on the "low" and "high" frequency ranges. Most of the COV are below 0.2, with only one value exceeding the 0.3 threshold.

3. Results

All the results presented in this section are normalized using the amplitude of the spectrum of the shaker force. Therefore, the quantity MSV is the mean square mobility rather than velocity, and p is the pressure transfer function.

3.1. Narrowband results

The curves in Figs. 10 and 11 show the MSV calculated on the plate in narrowband (frequency resolution = 0.1 Hz) when one to four ABHs are progressively added. The pictures show the peaks' mitigation effect in the low-frequency interval 50–400 Hz, in dry and wet conditions, respectively. The blue-coloured areas highlight the positive MSV

Table 4
Experimental tests performed in the deep-tank facility.

Test number	Label	Plate	Number of ABH	Model
1	Plt1	1	/	/
2	Plt2	2	/	/
3	AHB1L	1	1	2
4	ABH2L	1	2	2
5	ABH3L	1	3	2
6	ABH4L	1	4	2
7	ABH4S	2	4	1

Table 5
Coefficient of variation for tests Plt1, Plt2, ABH2L, and ABH4S averaged on ranges 50 ∇· 400 Hz and 500 ∇· 5000 Hz.

Range [Hz]	Set	Coefficient of variation (COV)			
		Plt1	PLt2	Plt1 ABH2L	Plt2 ABH4S
50–400	1	0.17	0.09	0.04	0.10
	2	0.14	0.08	0.08	0.07
500–5000	1	0.26	0.15	0.13	0.32
	2	0.19	0.15	0.17	0.13

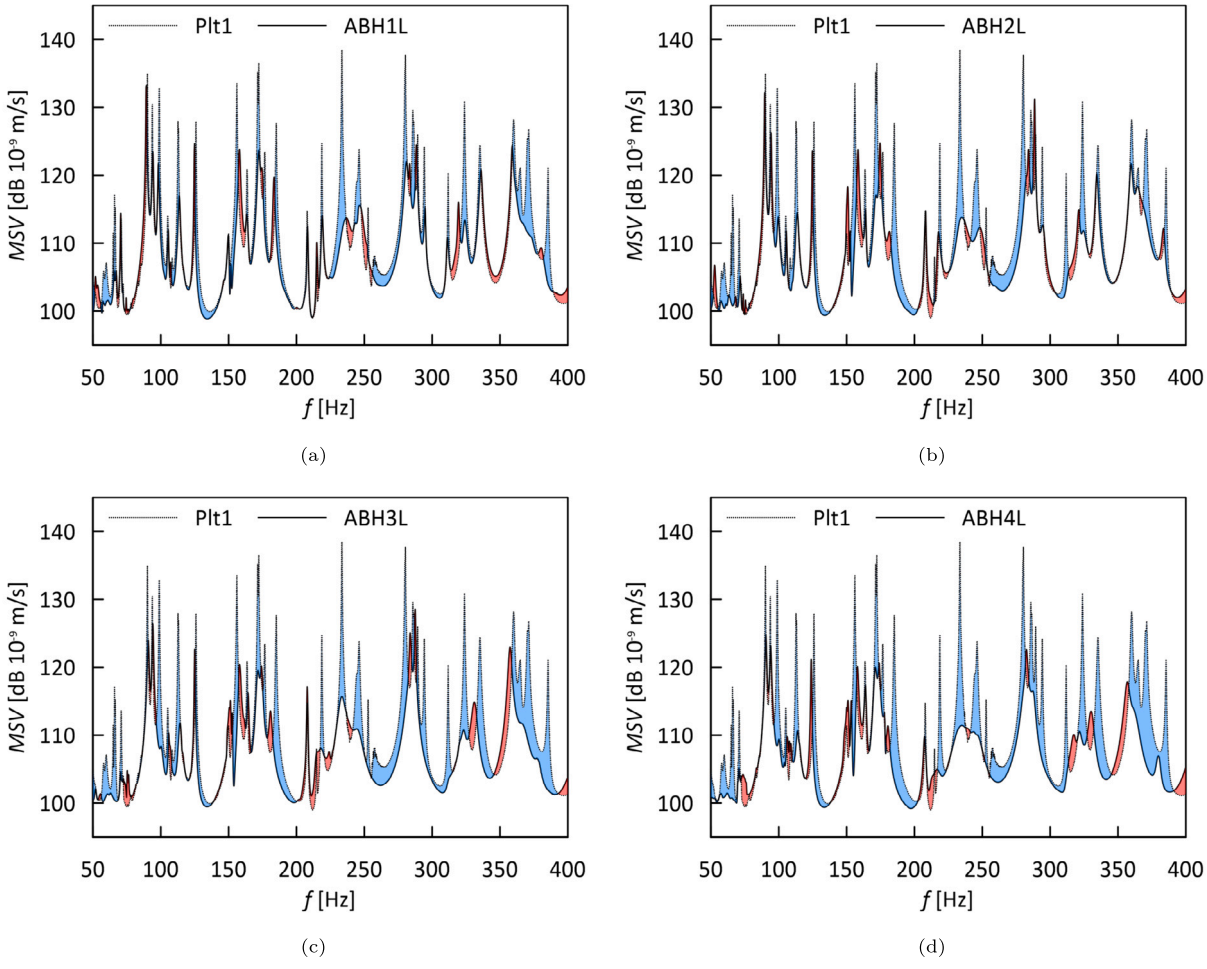

Fig. 10. Narrowband MSV between 50 Hz and 400 Hz adding progressively one (a), two (b), three (c), and four (d) ABH Model 2. Dry condition. The differences are evaluated with reference to the case Plt1.

differences between each pair of configurations plotted, while the red areas indicate a negative difference.

Figs. 12 and 13 show the effect obtained in dry and wet conditions, respectively, on the third-octave bands (800, 1000, and 1250 Hz) used for defining the position of the ABHs. These curves are related to the conditions "plate" and "ABH4", the frequency resolution used is 1 Hz. Curves on the left were obtained by using ABH Model 1, and curves on the right were obtained by using ABH Model 2. The blue areas indicate a decrease in the vibration, and the red areas indicate an increase. A general positive outcome can be observed in all the selected intervals, except for the configuration "ABH4L" when the plate is in water (Fig. 13(b)).

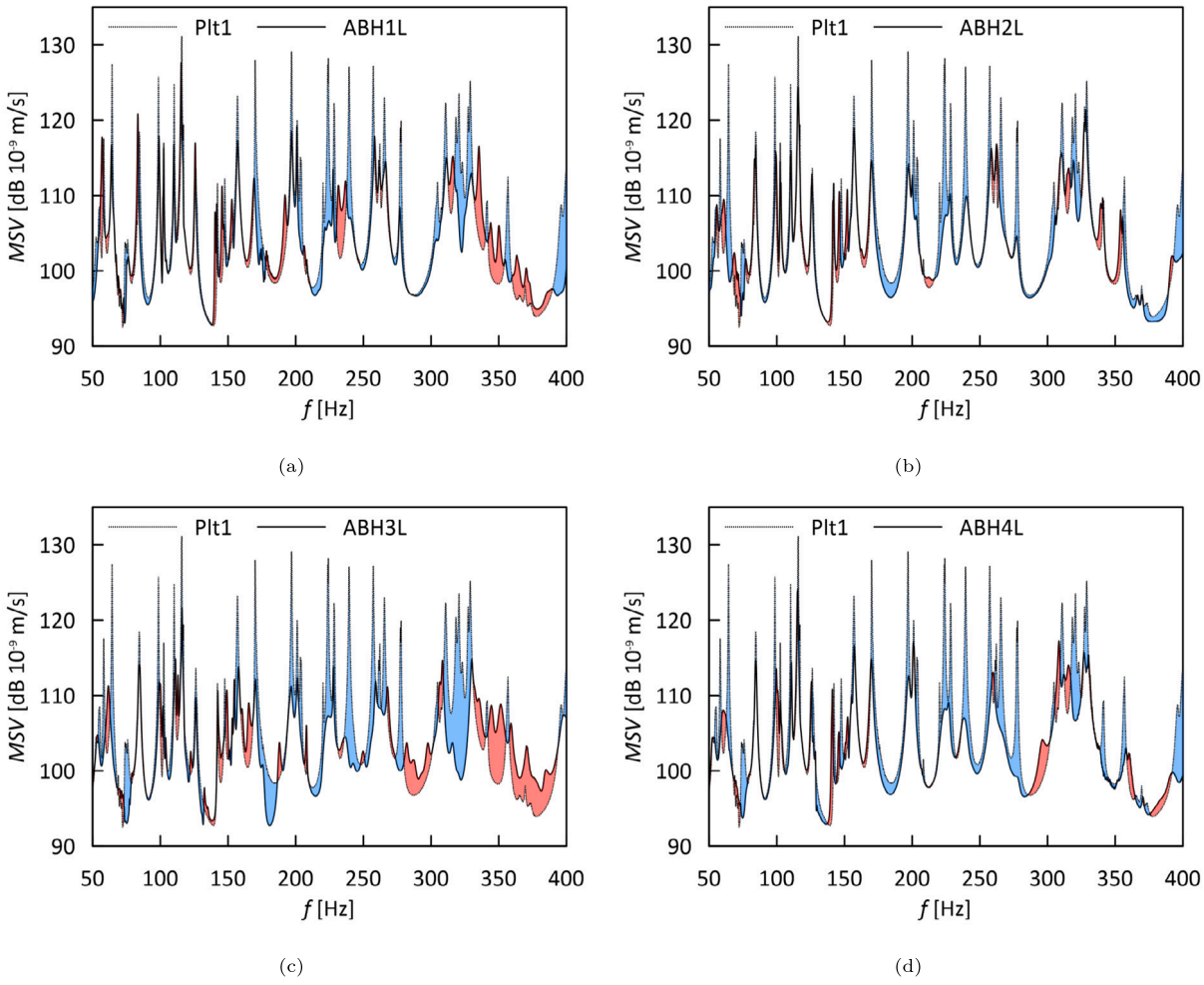

Fig. 11. Narrowband MSV between 50 Hz and 400 Hz adding progressively one (a), two (b), three (c), and four (d) ABH Model 2. Wet condition. The differences are evaluated with reference to the case Plt1.

3.2. Broadband results

The results observed in narrowband are analogous to the broadband ones. Figs. 14 and 15 show the gain obtained by each different configuration tested in the two conditions investigated. Reference is made with the case without ABH. In general, the ABH Model 2 gives better results below 500 ÷ 600 Hz, while, above it, ABH Model 1 gives the best performance. In dry condition, above the estimated cut-on frequency of 100 Hz, the gains are almost always positive or non-negative for both models. The same does not happen in wet condition, where, while using ABH Model 1 lead to a positive gain, when the Model 2 is used, a negative result is obtained above 600 Hz (Fig. 15).

The MSV differences obtained by adding four ABHs to the plate are shown by Figs. 16(a) and 16(b), divided by model used. Using Model 1 (Fig. 16(a)) the result obtained in air and water is similar, showing two spikes in the gain around the 125 Hz and 1000 Hz third-octave bands. Overall, the difference is almost always positive (except for 630 Hz third-octave band in dry condition). The consistency shown by the ABH Model 1 does not stand for Model 2 (Fig. 16(b)).

The cumulative results were also calculated. Table 6 indicates the differences obtained from the configurations with no ABHs and those with the ABHs installed. In the low-frequency interval, both models have a positive effect. When using Model 2, the table shows increased gains as progressively ABH are added to the plate in both air and water. In the high-frequency interval, Model 1 leads to a positive outcome, while Model 2 gives positive results in dry condition and negative results in wet condition. The gains increase or decrease as ABHs are progressively added. Overall, the outcome is positive in the 50–5000 Hz interval; depending on the condition, using Model 1 or Model 2 may be more advantageous.

3.3. Underwater sound pressure

The sound pressure measured was divided by the excitation force recorded by the load cell to obtain the pressure-to-force transfer function. Because of the characteristics of the facility, the results are plotted from the third-octave bands above 500 Hz. Fig. 17 shows the differences obtained for each condition for the two positions P_1 and P_2. The differences are obtained by subtracting from the levels measured in conditions Plt1 and Plt2, the levels obtained by installing the ABHs. The values are mostly negative, meaning that the ABHs worsen the performance of the plate in the interval between 500 and 5000 Hz.

4. Discussion

4.1. ABH performance

The primary objective of the experiment was to investigate the ABH potential in decreasing the plate's vibration and radiated pressure above the cut-on frequency. In the low-frequency range, below 400 ÷ 500 Hz, Model 2 outperforms Model 1, as indicated by the results in Figs. 14 and 15 and by comparing the overall gains in Table 6. The configuration having four ABH Model 2 installed, in the 10–400 Hz range, leads to a gain, in the two conditions, of 2.6 dB and 3.1 dB higher

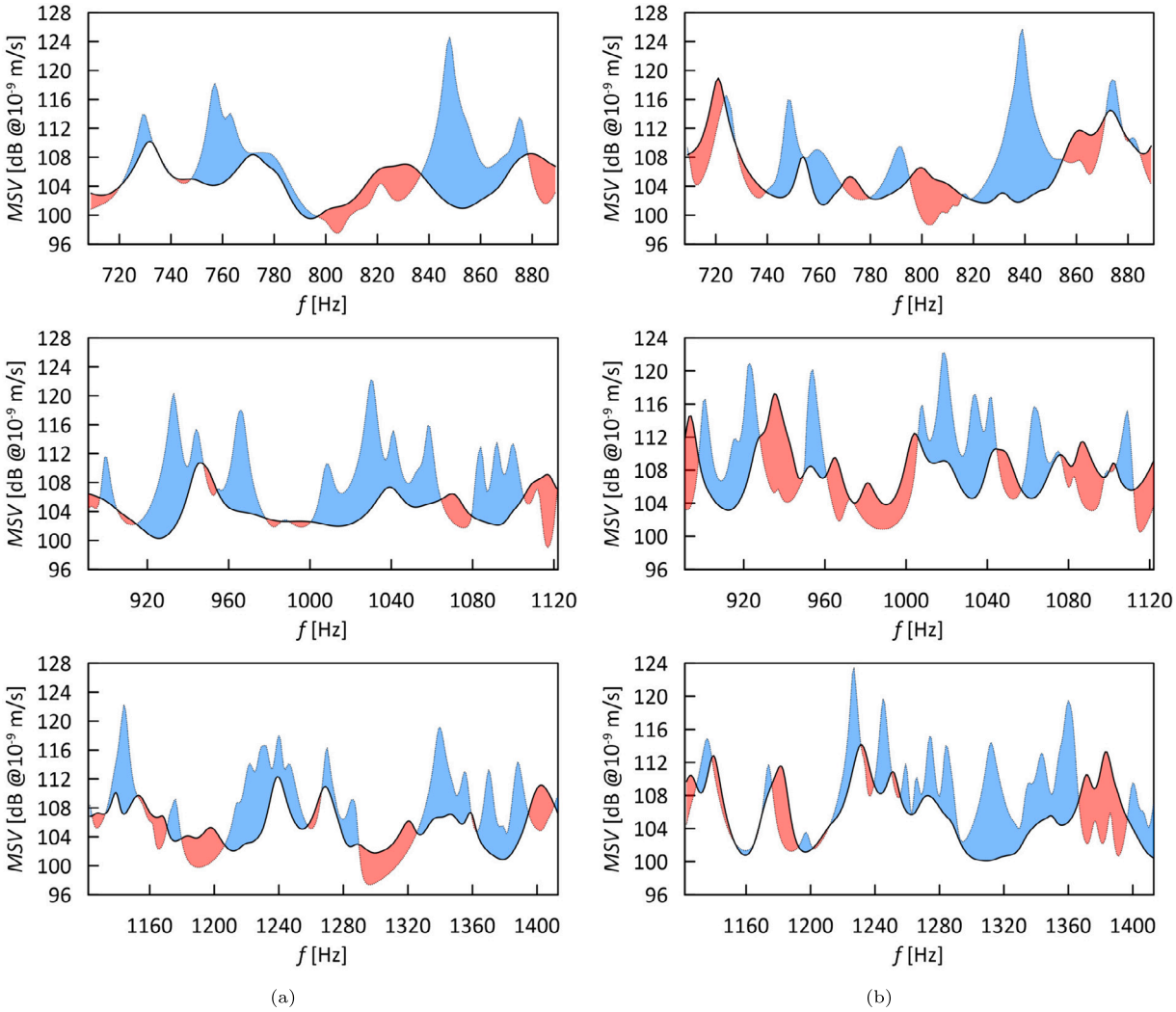

Fig. 12. Comparison between the MSV for the 800, 1000, and 1250 Hz third-octave bands calculated in dry condition on the plate before and after installing four ABHs: (a) Model 1, (b) Model 2. The differences are evaluated with reference to the case Plt2 and Plt1, respectively.

Table 6
Cumulative MSV level gains.

Condition	Interval [Hz]	ΔMSV [dB @ 10^{-9} m/s]				
		ABH1L	ABH2L	ABH3L	ABH4L	ABH4S
Dry	50–400	4.4	4.5	5.0	5.8	3.2
	400–5000	1.3	1.8	2.4	2.8	3.7
	50–5000	2.6	3.0	3.5	4.0	3.4
Wet	50–400	3.7	3.9	4.5	5.4	2.3
	400–5000	0	−0.7	−0.8	−1.0	3.2
	50–5000	2.0	1.7	1.8	1.8	2.7

than those obtained by Model 1. ABH Model 1 performance exceeds Model 2 only in the 125 and 160 Hz third-octave bands.

In the curves of the plate's narrowband MSV, the low-frequency interval shows a reduction in the number of modal peaks as the number of ABHs increases. This effect starts to be visible around 100 Hz, which is the estimated cut-on frequency calculated by Eq. (7). The progressive effect due to the addition of ABHs (Figs. 10 and 11) shows that most of the peaks are already affected by the first ABH installed. The subsequent ABHs adjoined increase the performance, but their relative contribution becomes less significant, depending on the installation position. This effect can be observed in Table 6: the gain obtained in the 10–400 Hz interval by installing the first ABH (Model 2) is 4.4 dB in dry condition and 3.7 dB in wet condition. By progressively adding the second, third, and fourth ABH, the gains obtained after the installations are 0.1, 0.5, and 0.8 dB for dry condition and 0.2, 0.6, and 0.9 dB for wet condition. The analysis of these values indicates that position S2 is redundant with respect to S1, while position S4 leads to a substantial decrease of the MSV.

In the high-frequency range, the ABH Model 1 has a better performance than Model 2, with the latter producing a worsening effect when the plate is in contact with the water. For both models, above 400 Hz, the modal behaviour of the plate is a combination of several modes of vibration. It is harder to control the dynamics of the plate using only 1–4 ABHs because the energy is distributed across the plate. A

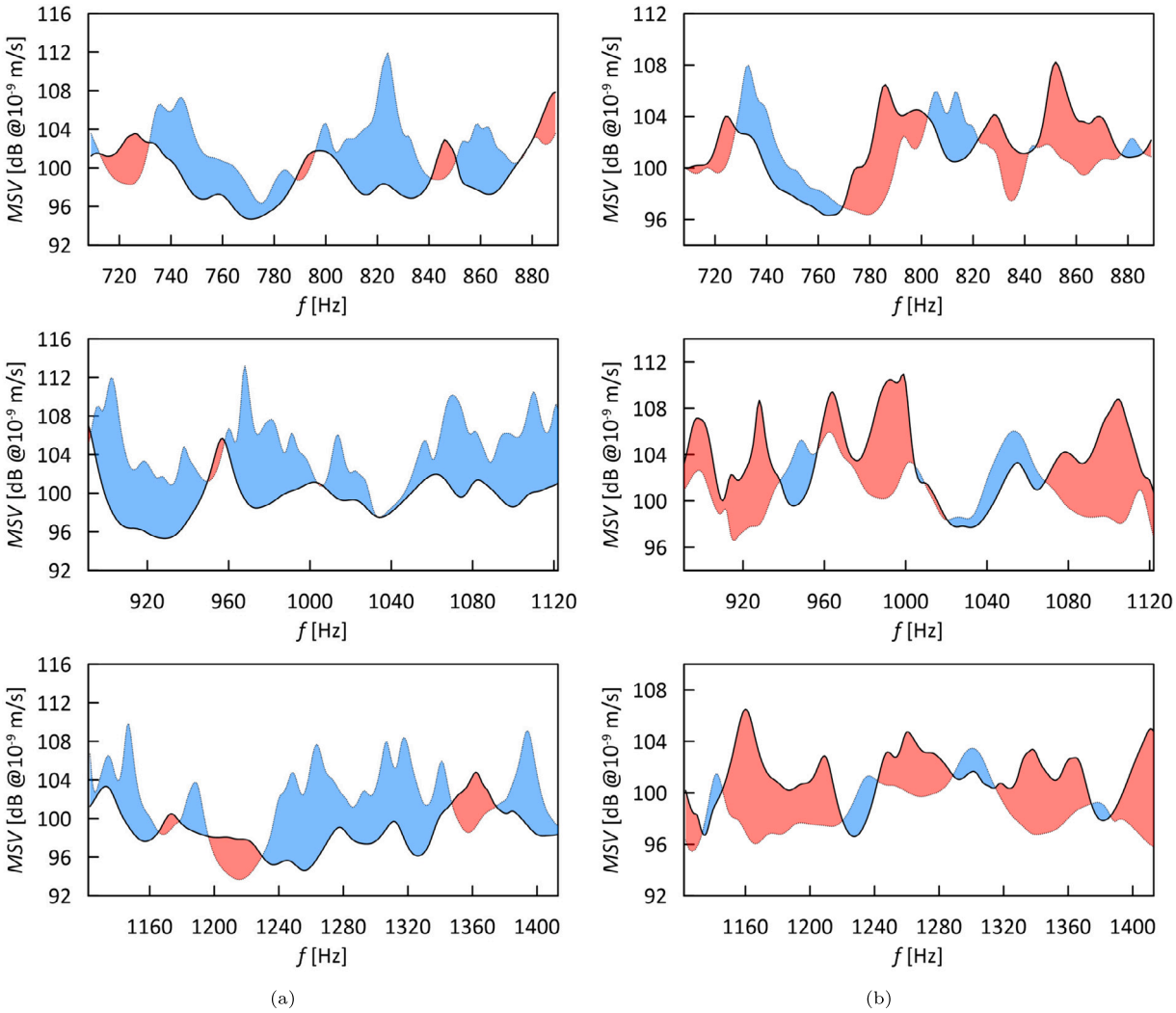

Fig. 13. Comparison between the MSV for the 800, 1000, and 1250 Hz third-octave bands calculated in wet condition on the plate before and after installing four ABHs: (a) Model 1, (b) Model 2. The differences are evaluated with reference to the case Plt2 and Plt1, respectively.

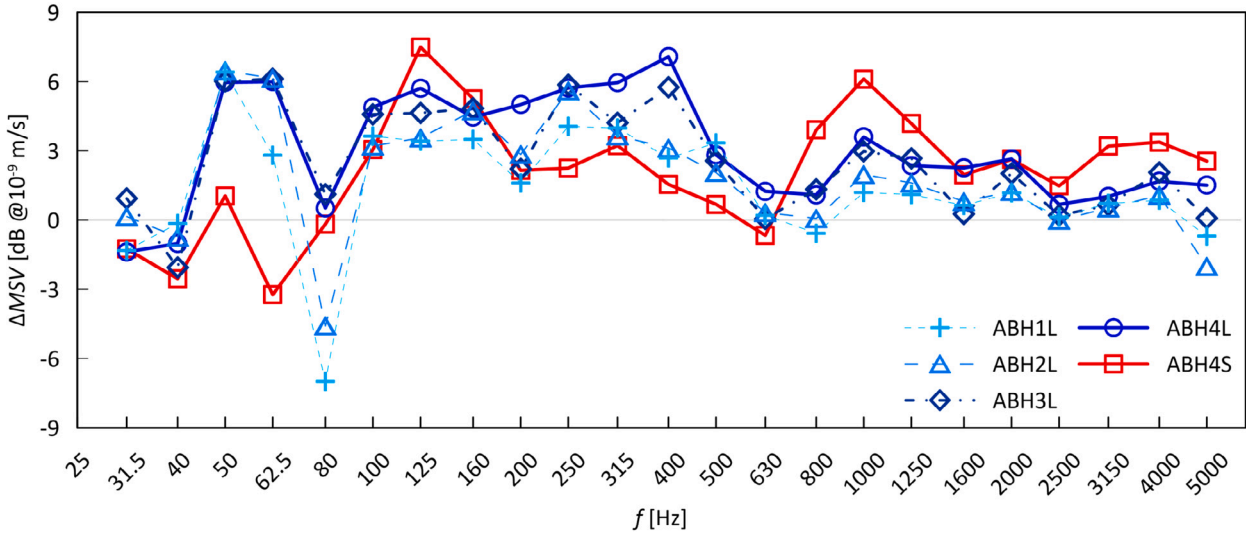

Fig. 14. MSV difference obtained in dry condition installing on the plate one, two, three, and four ABHs.

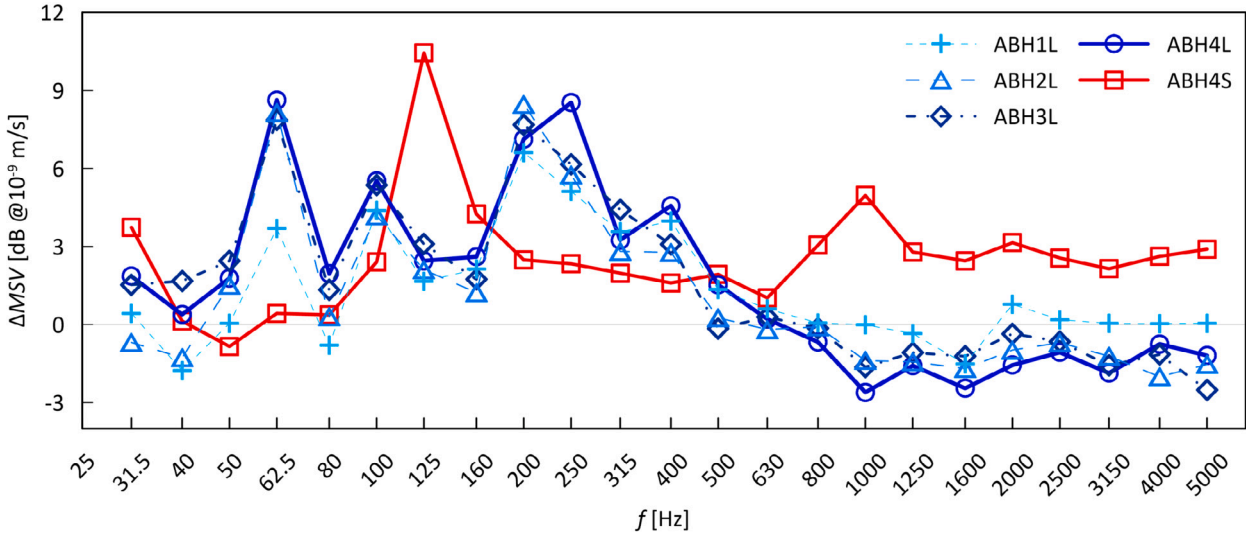

Fig. 15. MSV difference obtained in wet condition installing on the plate one, two, three, and four ABHs.

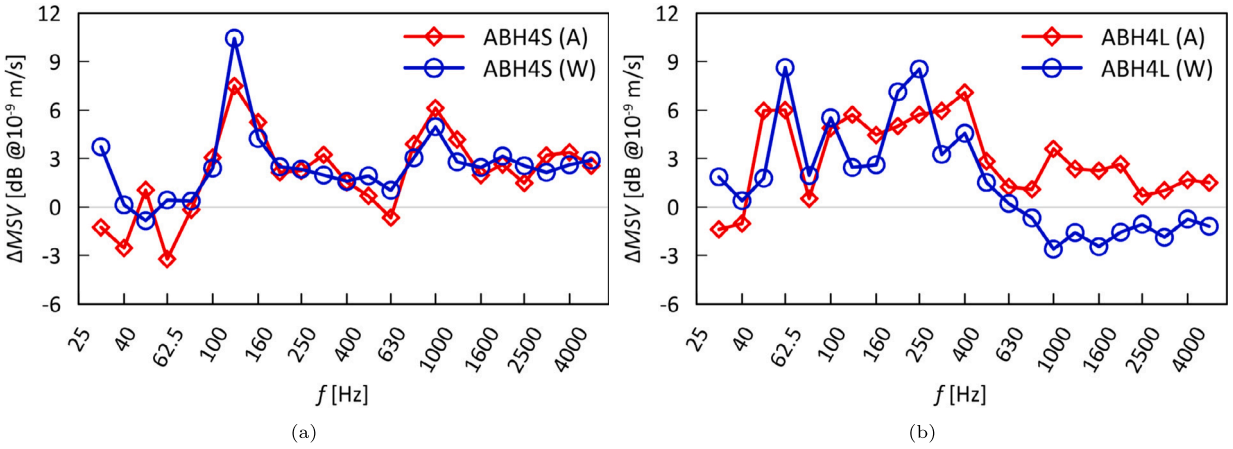

Fig. 16. MSV difference obtained installing four ABH in dry (A) and wet (W) condition: (a) Model 1, (b) Model 2.

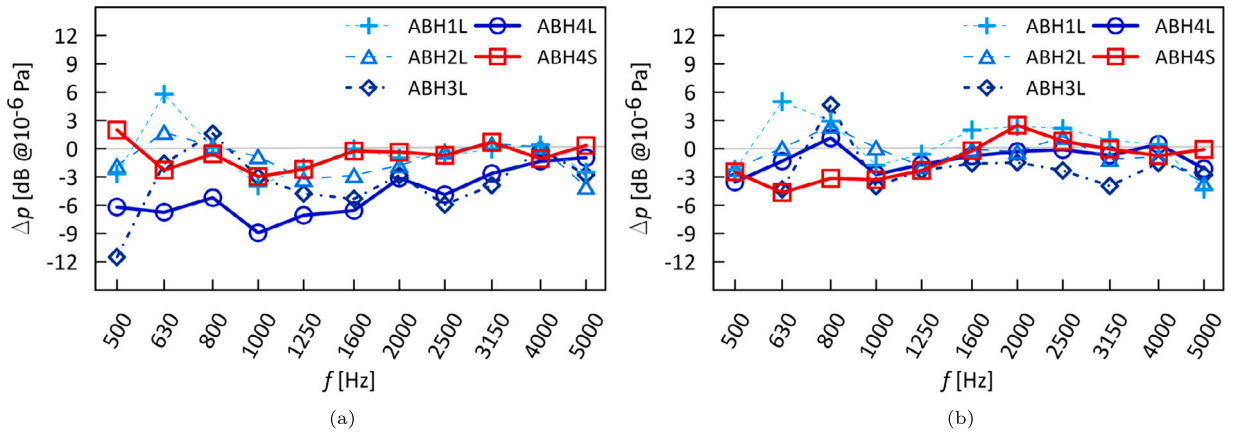

Fig. 17. Underwater pressure differences between the condition with no ABH and those with ABH installed for positions $P1$ (a) and $P2$ (b)

more appropriate solution would be a more diffuse system comprising many smaller ABHs. The different behaviour between the two models must be attributed to the 100 mm extension that differentiates them. The better performance of Model 2 in the lower frequency interval may be connected to the presence of an internal mode of vibration around 220 Hz. The same mode is estimated to be around 490 Hz for Model 1, as indicated by Table 2. We know that the modes of vibration of the ABH correspond to the frequencies of maximum dissipation of the device as the reflection coefficient drops to near zero. This explains why a longer ABH is more effective at lower frequencies. However,

Model 2's mode number also increases over 400 Hz, compared to Model 1. Therefore, following this logic, it should also perform better in the high-frequency range.

4.2. Hypothesis on ABH model 2 non linear behaviour

A hypothesis behind the inconsistent behaviour of ABH Model 2 may be found in a paper by Denis et al. (2017). The authors investigated the influence of adding a constant thickness extension to the ABH, pointing out that it improves some non-linear effects that naturally occur in the ABH. In particular, they observed a transfer of energy from the lower to the higher frequencies triggered by the presence of the extension. This phenomenon increases the vibration reduction performance of the ABH in the low-frequency range, as some energy, moving to higher frequencies, gets more efficiently dissipated. However, they also observed that adding viscoelastic material to the extension should eliminate these non-linear effects, leading back to the known linear ABH behaviour. The investigation by Denis et al. was performed numerically; in real situations, the non-linear effects may be enhanced even when a VEM layer covers the tip.

Assuming that the outcome of the paper (Denis et al., 2017) applies to our case, energy is transferred to higher frequencies in the response of Model 2. This should make the ABH more effective in the low-frequency range, which is what happens in dry condition. The difference in performance should be attributed to the interaction between the plate surface and the water. In wet conditions, the fluid–structure interaction effect causes an increase in the system's damping above 400 ÷ 500 Hz (Rognoni et al., 2024). Due to the high damping in this range, the surface vibration decrease due to addition of ABHs is very limited. On the contrary, the energy transfer described by Denis et al. (2017) could translate in a increase of the vibration in the high-frequency range if the energy moving from low to high frequency is greater than that entering and being dissipated by the ABH.

The energy balances could explain the peculiar effect of the ABH Model 2. We can suppose that the vibrational energy enters the ABH for frequencies above the cut-on frequency. Let us consider two flexural waves having frequencies ω_1 and ω_2 with $\omega_2 > \omega_1$. Some of their energy will enter the ABH, E_1 for wave 1 and E_2 for wave 2. Due to the reflection at the tip of the ABH, the energies E_1' and E_2' normally flowing back to the plate will be:

$$\begin{cases} E_1' = E_1 \cdot R_1 \\ E_2' = E_2 \cdot R_2 \end{cases} \tag{11}$$

with R_1 and R_2 the reflection coefficients at ω_1 and ω_2. Assuming there is a quantity of energy e that is transferred in the ABH from lower to higher frequency, the balance of energy flowing out is:

$$\begin{cases} E_1' = (E_1 - e) \cdot R_1 \\ E_2' = (E_2 + e) \cdot R_2 \end{cases} \tag{12}$$

When the energy balance relevant to wave 2, which is $E_2 - (E_2 + e) \cdot R_2$, is positive, it means that the energy flowing in is greater than that flowing out. This is verified when:

$$E_2 \cdot [(1 - R_2)/R_2] > e \tag{13}$$

and corresponds to the condition where the ABH absorbs energy from the host structure, as in the dry condition. The net effect obtained is an energy reduction in the structure on both frequencies ω_1 and ω_2. When Eq. (13) is not verified, the net energy balance becomes negative, leading to an increase in the energy and, therefore, of the vibration. Let us think of the limit case when the plate vibrations at ω_2 are totally damped by the water interaction ($E_2 = 0$): in this case, no energy is entering the ABH, but some energy is flowing out ($E_2' > 0$). This is what may happen in wet conditions, where the plate is already heavily damped by the fluid, preventing a significant amount of energy from being absorbed by the ABHs. In that case, the only effect the ABHs will have is to generate and transfer more energy to the plate below, energy which entered the device at lower frequencies.

4.3. Radiated pressure

The last objective of the experiment was to see if the ABHs could achieve a MSV reduction in three specific third-octave bands, namely 800, 1000, and 1250 Hz. This would have led to a decrease in the radiated power, according to Eq. (3). Figs. 12 and 13 show that the installation of ABH Model 1 reduces most of the peaks in the three intervals considered; the installation of ABH Model 2 reduces the MSV in dry condition but increases the plate vibration in wet condition (the increase was already discussed). The effect of the ABHs on the third-octave bands investigated can also be observed from Figs. 14 and 15. It must be noted that the ABH in position S1 does not have a particular effect on the 800 Hz band, the ABH in position S2 have little impact on the 1000 Hz band, the ABH in position S3 also has small effect on the 1250 Hz band, while the ABH in position S4 does not have much effect on any of the three bands, as expected. We can conclude that the positioning criterion used does not lead to a corresponding decrease of vibration in the target third-octave band, probably because the mode density is too high, while the positioning is based on a deterministic approach.

The radiated pressure was analysed above 500 Hz, a frequency considered a practical threshold for the tank, showing no positive effect of the installation on the ABH. The hydrophone in position P_1, in particular, showed negative differences between the response of the plate and those obtained with the ABHs Model 2 in most of the third-octave bands between 500 and 5000 Hz. Model 1 ABHs do not improve the situation either; the differences are negative or close to zero. The hydrophone in position P_2 shows that the ABH impact is generally negligible or negative.

4.4. Limitations of the study

By a general overview, the ABHs achieved good results in terms of a decrease in the plate MSV across the intervals investigated, with the exception of the effect of Model 2 in the high-frequency range when the plate is in wet condition. The same cannot be concluded for the plate radiated power, as no decrease in the levels was observed. The reason for the poor performance of the ABHs may be found in the testing configuration of the plate. We expected that the radiated power would be proportional to the mean square velocity measured on the plate surface, according to Eq. (3). However, Nilsson and Liu (2015) points out that for point-excited plates with a fluid loading on one side and below the coincidence frequency, the radiation from the bending near field dominates over the radiation from the reverberant field. The time-averaged radiated power by the plate is due to the displacement at and very close to the excitation point. It depends on the average value of the force $\bar{F}$ and the wavenumber k of the wave radiated into the fluid.

$$P_{rad} = \frac{|\bar{F}|^2 k^2}{6\pi c \rho} \tag{14}$$

Eq. (14) shows that the radiated acoustical power is not a function of the plate's material parameters but only of fluid properties and frequency. There is no dependency on the loss factor η of the system, meaning that additional damping will have little effect on the radiated power, although Junger and Feit (1986) specified that this condition is true above a certain value of the loss factor:

$$\eta_{limit} > \frac{8\rho\sqrt{1+\beta^{-2}}}{k\kappa^2\, mA}\left[1+\beta\left(\frac{f_c}{f}-1\right)^{-\frac{1}{2}}\right]^{-\frac{3}{2}} \tag{15}$$

where $\beta = \rho c/2\pi f \cdot m$, f_c is the coincidence frequency, f the frequency, m the mass of the plate, and κ is the plate wavenumber. Above this value, even if the addition of damping will significantly reduce the plate MSV, this will not lead to an equal reduction in the sound radiated. Rognoni et al. (2024) estimated the plate damping in wet condition.

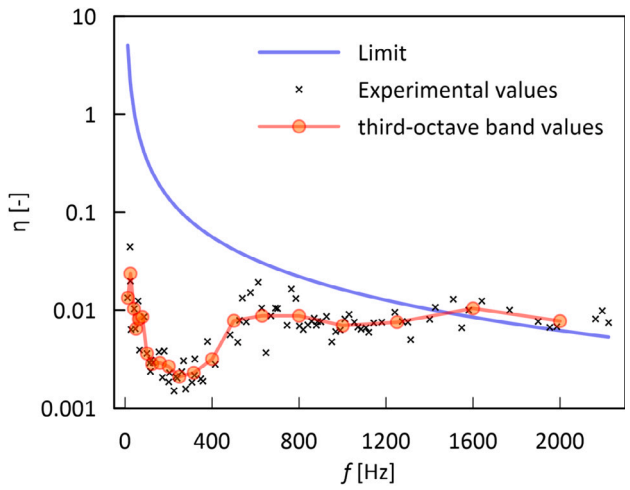

Fig. 18. Experimental loss factor of the plate in water compared with the limit given by Eq. (15).

Fig. 18 compares its third-octave band values with the limit given by Junger and Feit in the frequency range 0–2250 Hz.

Assuming Junger and Feit's condition is true, it would mean that, above 1500 Hz, any damping added to the plate will not decrease radiated power. Observing the radiated pressure by the plate when the ABHs Model 1 is installed (Fig. 17), this hypothesis stands. However, before 1500 Hz, where the added damping should mitigate the noise, the hypothesis fails, as the radiated pressure difference is negative. Regarding Model 2, the differences are almost always negative, indicating that the ABH installed generates more noise rather than decreases it. They may work as additional sound sources due to the non-linear energy transfer mechanism between low and high frequencies. This indicates the negative impact of the constant thickness extension added to Model 2 in the high-frequency range.

Other negative effects are linked to modes that may be introduced in the plate dynamics by the ABH dynamics. The narrowband curves shown in Section 3.1 have red areas indicating the negative difference before and after installing the ABH. Even if, overall, the gains obtained in a frequency interval may be positive, they may be specific frequencies where the effect is opposite. This aspect must be taken into account when considering the use of external ABH.

5. Conclusion

The experiment showed the potential of ABHs in mitigating the structural vibrations of a plate in contact with water. The effect of ABHs on the plate in air (dry condition) confirmed the results found in scientific literature on the subject. In wet condition, the outcome was different depending on the ABH used and the frequency range analysed. Below 400 Hz, both models decreased the MSV; above 400 Hz, the result was positive using Model 1 and negative using Model 2. This indicates an influence of the water on the performance of the ABHs installed on the plate.

With reference to the real case of a ship hull, a reduction in vibration is expected to generate a decrease of the URN, as the latter is generally caused by modal radiation (Nilsson and Liu, 2015). In our experiment, the recorded reduction of plate vibration did not correspond to a reduction of radiated noise in the tank. The difference between these two outcomes was attributed to the peculiar condition of the point-excited plate we used in the laboratory test. This conclusion led us to formulate a hypothesis on the limitations of the study expose in Section 4.4.

As for the number of ABHs, the results show that placing fewer ABHs in the right spots is more important than having more devices in locations that do not affect the plate dynamics. The disposition of ABHs must be optimized for the selected target frequency interval. In general, however, using from two to three ABHs decreases the MSV from 3 to 9 dB, depending on the third-octave band selected. This vibration decrease effect is obtained with an added weight between 3 and 3.5 kg, corresponding to an increase of total plate weight of about 4% and 5%.

Future developments of this investigation should be directed to assessing radiated noise reduction on structures more similar to ship hull plating. Different excitation and boundary conditions applied to the structure must be considered. Further analysis should be conducted to assess the low-frequency efficiency of ABH in decreasing the underwater radiated noise. Numerical models can also be used to predict the ABH performance, reducing the experimental effort.

CRediT authorship contribution statement

Giovanni Rognoni: Writing – original draft, Methodology, Investigation, Formal analysis, Data curation, Conceptualization. **Jacopo Fragasso:** Writing – original draft, Validation, Supervision, Investigation, Data curation. **Marco Biot:** Supervision, Resources, Methodology, Funding acquisition, Data curation, Conceptualization. **Lorenzo Moro:** Writing – review & editing, Validation, Supervision, Resources, Funding acquisition, Conceptualization.

Acknowledgements

Results achieved with the funding obtained under the Axis IV of PON Research and Innovation 2014–2020 "Education and research for recovery – REACT-EU"

Declaration of competing interest

The authors declare that they have no known competing financial interests or personal relationships that could have appeared to influence the work reported in this paper.

References

Aklouche, O., Pelat, A., Maugeais, S., Gautier, F., 2016. Scattering of flexural waves by a pit of quadratic profile inserted in an infinite thin plate. J. Sound Vib. 375, 38–52. http://dx.doi.org/10.1016/j.jsv.2016.04.034.

American Bureau of Shipping, 2024. Underwater noise and external airborne noise.

Bosschers, J., Boucheron, R., Pang, Y., Park, C., Pearce, B., Sipila, T., Tersta, C., Viviani, M., 2021. The Specialist Committee on Hydrodynamic Noise: Final Report and Recommendations to the 29th ITTC.

Bschorr, O., Raida, H.J., 2022. One-way vibration absorber. Acoustics 4 (3), 554–563. http://dx.doi.org/10.3390/acoustics4030034, URL: https://www.mdpi.com/2624-599X/4/3/34.

Bureau Veritas, 2018. Underwater radiated noise.

Conlon, S.C., Fahnline, J.B., Semperlotti, F., 2015. Numerical analysis of the vibroacoustic properties of plates with embedded grids of Acoustic Black Holes. J. Acoust. Soc. Am. 137, 447–457. http://dx.doi.org/10.1121/1.4904501.

CR Classification Society, 2023. Guidelines for Underwater Radiated Noise.

Deng, J., Gao, N., Chen, X., Pu, H., Guo, J., 2023. Underwater sound radiation from a Mindlin plate with an acoustic black hole. Ocean Eng. 278, http://dx.doi.org/10.1016/j-oceaneng.2023.114376.

Deng, J., Guasch, O., Maxit, L., Zheng, L., 2021. Transmission loss of plates with multiple embedded Acoustic Black Holes using statistical modal energy distribution analysis. Mech. Syst. Signal Process. 150, 107262. http://dx.doi.org/10.1016/j.ymssp.2020.107262.

Denis, V., Pelat, A., Touzé, C., Gautier, F., 2017. Improvement of the Acoustic Black Hole effect by using energy transfer due to geometric nonlinearity. Int. J. Non-Linear Mech. 94, 134–145. http://dx.doi.org/10.1016/j.ijnonlinmec.2016.11.012.

Det Norske Veritas Germanischer Lloyd, 2010. Silent class notation.

Du, X., Huang, D., Fu, Q., Zhang, J., 2019. Effects of Acoustic Black Hole parameters and damping layer on sound insulation performance of ABH circular plate. Appl. Sci. 9, http://dx.doi.org/10.3390/app9245366.

EU Commission, 2024. Commission Notice on the threshold values set under the Marine Strategy Framework Directive 2008/56/EC and Commission Decision (EU) 2017/848.

Feurtado, P.A., Conlon, S.C., 2016. An experimental investigation of Acoustic Black Hole dynamics at low, mid, and high frequencies. J. Vib. Acoust. 138, http://dx.doi.org/10.1115/1.4033894.

Feurtado, P.A., Conlon, S.C., 2017. Transmission loss of plates with embedded Acoustic Black Holes. J. Acoust. Soc. Am. 142, 1390–1398. http://dx.doi.org/10.1121/1.5001503.

Fragasso, J., Helal, K.M., Moro, L., 2024. Transfer-path analysis to estimate underwater radiated noise from onboard structure-borne sources. Appl. Ocean Res. 147, 103979. http://dx.doi.org/10.1016/j.apor.2024.103979.

Gaggero, S., Gaggero, T., Tani, G., Villa, D., Rizzuto, E., Pinto, O., Becchi, P., De Angelis, E., Viviani, M., 2025. Propeller design by optimisation for underwater radiated noise reduction: a full scale application. Ocean Eng. 333, 121412. http://dx.doi.org/10.1016/j.oceaneng.2025.121412.

Gao, N., Zhang, Z., Li, Y., Pan, G., 2025. Experimental verification of ultra-broadband vibration reduction of underwater vehicle pressure-resisting shells using Acoustic Black Holes. Thin-Walled Struct. 211, 113118. http://dx.doi.org/10.1016/j.tws.2025.113118, URL: https://www.sciencedirect.com/science/article/pii/S0263823125002125.

Gavrić, L., Pavić, G., 1993. A finite element method for computation of structural intensity by the normal mode approach. J. Sound Vib. 164, 29–43. http://dx.doi.org/10.1006/jsvi.1993.1194, URL: https://www.sciencedirect.com/science/article/pii/S0022460X83711946.

Government of Canada, 2024. Canada's ocean noise strategy. https://waves-vagues.dfo-mpo.gc.ca/library-bibliotheque/41255987.pdf. (Accessed 12 January 2026).

Hambric, S.A., Fahnline, J.B., 2016. Sound-structure interaction fundamentals. In: Engineering Vibroacoustic Analysis. John Wiley and Sons, Ltd, pp. 88–113. http://dx.doi.org/10.1002/9781118693988.ch4, arXiv:https://onlinelibrary.wiley.com/doi/pdf/10.1002/9781118693988.ch4.

Hildebrand, J.A., 2009. Anthropogenic and natural sources of ambient noise in the ocean. Mar. Ecol. Prog. Ser. 395, 5–20. http://dx.doi.org/10.3354/meps08353.

IMO, 2014. Guidelines for the Reduction of Underwater Noise from Commercial Shipping to Address Adverse Impacts on Marine Life.

IMO, 2023. Revised Guidelines for the Reduction of Underwater Noise from Commerical Shipping to Address Adverse Impacts on Marine Life.

Islam, M.S., 2022. Measurements of Underwater Radiated Noise from Non-Cavitating Propellers in Atmospheric Towing Tank (Master thesis). Memorial University of Newfoundland, http://dx.doi.org/10.48336/YRR3-VJ47.

ISO, 2016. ISO 17208-1:2016 - Underwater Acoustics: Quantities and procedures for description and measurement of underwater sound from ships. Part 1: Requirements for precision measurements in deep water used for comparison purposesAcoustics.

ISO, 2019. ISO 17208-1:2019 - Underwater Acoustics: Quantities and procedures for description and measurement of underwater sound from ships. Part 2: Determination of source levels from deep water measurements.

Jeon, W., Son, T., Park, S., 2024. Lightweight waveguide absorbers based on spiral Acoustic Black Holes for reducing structural vibrations in mechanical systems. In: INTER-NOISE and NOISE-CON Congress and Conference Proceedings. http://dx.doi.org/10.3397/IN_2024_4344, 10013–10016(4).

Ji, H., Wang, X., Qiu, J., Cheng, L., Wu, Y., Zhang, C., 2019. Noise reduction inside a cavity coupled to a flexible plate with embedded 2-D Acoustic Black Holes. J. Sound Vib. 455, 324–338. http://dx.doi.org/10.1016/j.jsv.2019.05.004.

Ji, H., Wang, N., Zhang, C., Wang, X., Cheng, L., Qiu, J., 2021. A vibration absorber based on two-dimensional Acoustic Black Holes. J. Sound Vib. 500, http://dx.doi.org/10.1016/j.jsv.2021.116024.

Ji, H., Zhao, X., Wang, N., Huang, W., Qiu, J., Cheng, L., 2022. A circular eccentric vibration absorber with circumferentially graded Acoustic Black Hole features. J. Vib. Acoust. Trans. ASME 144, http://dx.doi.org/10.1115/1.4053475.

Jones, A.D., Hoefs, S.A., 1996. Acoustical Properties of the MOD Salisbury Test Tank and Techniques for Measurements. Technical Report DSTO-RR-0068, Defence Science and Technology Organization, Canberra (Australia).

Junger, M.C., Feit, D., 1986. Sound, Structures, and Their Interaction. MIT Press.

Korean Register, 2021. Guidances for Underwater Radiated Noise.

Kruger, D.H., Adin Mann, III, J., Wiegandt, T., 1997. Placing constrained layer damping patches using reactive shearing structural intensity measurements. J. Acoust. Soc. Am. 101 (4), 2075–2082. http://dx.doi.org/10.1121/1.418243, arXiv:https://pubs.aip.org/asa/jasa/article-pdf/101/4/2075/8082704/2075_1_online.pdf.

Krylov, V., 2014. Acoustic Black Holes: Recent developments in the theory and applications. IEEE Trans. Ultrason. Ferroelectr. Freq. Control 61, 1296–1306. http://dx.doi.org/10.1109/TUFFC.2014.3036.

Krylov, V., Winward, R., 2007. Experimental investigation of the Acoustic Black Hole effect for flexural waves in tapered plates. J. Sound Vib. 300, 43–49. http://dx.doi.org/10.1016/j.jsv.2006.07.035.

Lee, G.G., 1988. Analytical and Experimental Studies of Beam Waveguide Absorbers for Structural Damping (Master thesis). Naval Postgraduate School, Monterey, California, USA.

Lee, J.Y., Cho, D.S., Kim, K., Park, S.J., 2023. Experimental validation on structure-borne underwater radiated noise transfer function analysis for marine structure. Int. J. Nav. Arch. Ocean. Eng. 16, 100585. http://dx.doi.org/10.1016/j.ijnaoe.2024.100585, URL: https://www.sciencedirect.com/science/article/pii/S2092678224000049.

Lee, J.Y., Jeon, W., 2017. Vibration damping using a spiral Acoustic Black Holes. J. Acoust. Soc. Am. 141 (3), 1437–1445. http://dx.doi.org/10.1121/1.4976687, arXiv:https://pubs.aip.org/asa/jasa/article-pdf/141/3/1437/15319705/1437_1_online.pdf.

Lee, J.Y., Jeon, W., 2019. Exact solution of Euler-Bernoulli equation for Acoustic Black Holes via generalized hypergeometric differential equation. J. Sound Vib. 452, 191–204. http://dx.doi.org/10.1016/j.jsv.2019.02.016.

Lee, J.Y., Jeon, W., 2021. Wave-based analysis of the cut-on frequency of curved Acoustic Black Holes. J. Sound Vib. 492, http://dx.doi.org/10.1016/j.jsv.2020.115731.

Li, M., Deng, J., Zheng, L., Xiang, S., 2022. Vibration mitigation via integrated Acoustic Black Holes. Appl. Acoust. 198, 109001. http://dx.doi.org/10.1016/j.apacoust.2022.109001.

Lloyd's Register, 2018. Additional design and construction procedure for the determination of a vessel's underwater radiated noise.

Minonov, M.A., 1988. Elastic wave propagation in a plate, thickness of which smoothly decreases to zero on a finite interval. Akust. Zh. 34, 546–547, URL: http://www.akzh.ru/pdf/1988_3_546-547.pdf.

Nilsson, A., Liu, B., 2015. Vibro-acoustics, volume 2. Springer Berlin Heidelberg, Berlin, Heidelberg, http://dx.doi.org/10.1007/978-3-662-47934-6.

Park, S., Lee, J.Y., Jeon, W., 2022. Vibration damping of plates using waveguide absorbers based on spiral Acoustic Black Holes. J. Sound Vib. 521, http://dx.doi.org/10.1016/j.jsv.2021.116685, URL: https://www.sciencedirect.com/science/article/pii/S0022460X21006945.

Park, M.H., Yeo, S., Choi, J.H., Lee, W.J., 2024. Review of noise and vibration reduction technologies in marine machinery: Operational insights and engineering experience. Appl. Ocean Res. 152, 104195. http://dx.doi.org/10.1016/j.apor.2024.104195.

Pavić, G., 1976. Measurement of structure borne wave intensity, Part I: Formulation of the methods. J. Sound Vib. 49, 221–230. http://dx.doi.org/10.1016/0022-460X(76)90498-3, URL: https://www.sciencedirect.com/science/article/pii/0022460X76904983.

Pelat, A., Gautier, F., Conlon, S.C., Semperlotti, F., 2020. The Acoustic Black Hole: A review of theory and applications. J. Sound Vib. 476, http://dx.doi.org/10.1016/j.jsv.2020.115316.

Registro Italiano Navale, 2022. Ship rules 2022 Part F.

Rognoni, G., Moro, L., Biot, M., 2024. Model tuning of a vibrating plate in contact with water. Proc. Inst. Acoust. 46 (1).

Smith, T.A., Rigby, J., 2022. Underwater radiated noise from marine vessels: A review of noise reduction methods and technology. Ocean Eng. 266, http://dx.doi.org/10.1016/j.oceaneng.2022.112863.

Spalding, A.B., Mann, III, J.A., 1995. Placing small constrained layer damping patches on a plate to attain global or local velocity changes. J. Acoust. Soc. Am. 97 (6), 3617–3624. http://dx.doi.org/10.1121/1.412444, arXiv:https://pubs.aip.org/asa/jasa/article-pdf/97/6/3617/11574247/3617_1_online.pdf.

Tani, G., Viviani, M., Hallander, J., Johansson, T., Rizzuto, E., 2016. Propeller underwater radiated noise: A comparison between model scale measurements in two different facilities and full scale measurements. Appl. Ocean Res. 56, 48–66. http://dx.doi.org/10.1016/j.apor.2016.01.007.

Tao, Z., Cen, Y., Wu, H., Li, Q., Wang, Y., Lyu, H., Liu, J., Shang, L., 2025. Experimental investigation of train-induced vibration transmission to the high-rise building during different train operations. Buildings 15 (24), http://dx.doi.org/10.3390/buildings15244524, URL: https://www.mdpi.com/2075-5309/15/24/4524.

Tian, Y., Zhang, C., Yang, L., 2025. Active control of vibration and radiated noise in the shaft-shell coupled system of an underwater vehicle. Appl. Ocean Res. 154, 104324. http://dx.doi.org/10.1016/j.apor.2024.104324, URL: https://www.sciencedirect.com/science/article/pii/S0141118724004450.

Ungar, E.E., Kurzwell, L., 1984. Preliminary Evaluation of Waveguide Absorbers. Bolt Beranek and Newman Inc., 10 Moulton St., Cambridge, MA.

Watson, S.J., 1989. Experimental Studies of Circular Viscoelastic Waveguide Absorbers for Passive Structural Damping (Master thesis). Naval Postgraduate School, Monterey, California, USA.

Wen, H., Guo, X., Ma, R., Guo, J., Shi, Z., Ye, L., 2024. Vibration control mechanisms of plate structures by 1D acoustic black hole dynamic vibration absorber. Phys. Scr. 99 (5), 055268. http://dx.doi.org/10.1088/1402-4896/ad3e39.

Zhang, Y., Tong, M., Rui, X., Wang, G., Yang, F., Zhou, Q., Cheng, L., He, B., 2024. Ultrathin and pressure-resistant meta-coating with embedded tree-shaped Acoustic Black Hole for broadband low-frequency underwater sound absorption. Appl. Acoust. 225, 110171. http://dx.doi.org/10.1016/j.apacoust.2024.110171, URL: https://www.sciencedirect.com/science/article/pii/S0003682X24003220.

Zhao, X., Wang, C., Ji, H., Qiu, J., Cheng, L., 2024. Vibration reduction by a partitioned dynamic vibration absorber with Acoustic Black Hole features. Chin. J. Mech. Eng. 37 (75), http://dx.doi.org/10.1186/s10033-024-01049-x.

Zhou, T., Cheng, L., 2018. A resonant beam damper tailored with Acoustic Black Hole features for broadband vibration reduction. J. Sound Vib. 430, 174–184. http://dx.doi.org/10.1016/j.jsv.2018.05.047.